From two- to three-dimensional alumina: Interface templated films and formation of −Al2O3 (111) nuclei

Zabka, Wolf-Dietrich ; Leuenberger, Dominik ; Mette, Gerson ; Osterwalder, Jürg

DOI: https://doi.org/10.1103/PhysRevB.96.155420

From two- to three-dimensional alumina: Interface templated films and formation of γ-Al_2O_3(111) nuclei

Wolf-Dietrich Zabka,[1] Dominik Leuenberger,[1] Gerson Mette,[1,2] and Jürg Osterwalder[1]
[1]*Physik-Institut, Universität Zürich, Winterthurerstrasse 190, 8057 Zürich, Switzerland*
[2]*Fachbereich Physik, Philipps-Universität Marburg, Renthof 5, 35032 Marburg, Germany*
(Received 29 May 2017; revised manuscript received 27 July 2017; published 9 October 2017)

Oxide thin films are of fundamental importance due to their applications in materials science, optics, corrosion protection, catalysis, and microelectronics. A multistep oxidation procedure is employed to precisely tune the alumina (Al_2O_3) thickness on a NiAl(110) alloy from two atomic bilayers to 1.5 nm. Structural changes are analyzed with x-ray photoelectron diffraction and low-energy electron diffraction. The long-range order does not relate to any bulk structure and is imposed by the crystallized interface. The large unit cell formed at the interface persists in thicker films. In contrast, the local order changes at a thickness above 0.5 nm from the complex structure of this prelayer under the formation of subnanometer-sized γ-Al_2O_3(111)-type nuclei. The band structure is monitored with angle-resolved photoelectron spectroscopy. Increasing film thickness results in a slight decrease of the work function, but does not lead to significant changes of the electronic band structure. The presented multistep procedure opens a route for the synthesis of thin film structures in general and in particular provides fundamental insight in the surface structure of spinel-based transition Al_2O_3.

DOI: 10.1103/PhysRevB.96.155420

I. INTRODUCTION

Many oxide materials are electrically insulating, which renders the characterization of their surface properties difficult with most of the surface science tools that are typically electron or ion based [1]. This insulating character can be overcome by studying these materials in the form of a few atomic layer thick ultrathin films prepared on conducting substrates. In heterogeneous catalysis, this approach has been used extensively in the last decades and many of these model ultrathin oxide films were studied under ultrahigh vacuum (UHV) conditions with great control [2,3], providing fundamental insights into the structural and electronic properties of these materials [4].

However, the properties of ultrathin oxide films often deviate from their respective bulk counterparts [5], and can significantly change depending on the film thickness. This was demonstrated for gold adatoms on MgO ultrathin films epitaxially grown on Ag(100), where both the preferred adsorption site as well as the charge state can be altered by increasing the oxide film thickness [6–8]. Similar concepts also apply to molecules adsorbed on insulating ultrathin films: The gap between the highest occupied and lowest unoccupied molecular orbital as well as the charge transfer upon adsorption depend not only on polarization effects at the interface, but to a large extent also on the thickness of the insulating layer [9–11]. Catalytic activity can also change drastically in such systems: Recently, it was shown that due to changes in the electronic properties, the CO oxidation activity of palladium clusters deposited on alumina (Al_2O_3) films on Re(0001) strongly depends on the film thickness [12]. To fully understand which properties of the adsorbed species rely on the adsorbate/oxide interface and which are influenced by the underlying substrate material, the oxide thickness needs to be varied in a controlled manner [13].

Al_2O_3 is one of the most technologically relevant oxide materials. The stable bulk phase is α-Al_2O_3, also called corundum or sapphire. Several further metastable phases exist, e.g., γ-, δ-, θ-, χ-, κ-, κ'-, and η-Al_2O_3 [14]. γ-Al_2O_3 is of special technological importance, as it is the most frequently used catalyst support for hydrotreating [15]. Despite its relevance, the detailed structure of γ-Al_2O_3 is still under debate [14,16]. It is generally described as a defective spinel structure, however, no general agreement exists on the detailed location of cation vacancies and the occupation of interstitial sites [14,16]. Recently, the growth of well-defined crystalline (100)-oriented spinel alumina films was demonstrated on a $MgAl_2O_4$(100) surface [17]. They deliver a satisfactory model system for spinel-based transition alumina (γ-, δ-, and η-Al_2O_3) [17], but the insulating nature of the $MgAl_2O_4$ substrate limits its application as a model system.

A viable approach for the synthesis of ultrathin oxide films is based on the selective oxidation of suitable bimetallic alloys [18–22]. The prototypical example is an ultrathin alumina film on the NiAl(110) substrate [18,23], which has been widely used as a support in model catalytic studies [1,24–26]. This ultrathin surface oxide has an $Al_{10}O_{13}$ stoichiometry, consists of two atomic bilayers, and has $O_{s7}{}^{2-}$ $Al_{s6}{}^{3+}$/$O_{i6}{}^{2-}$ $Al_{i4}{}^{2+}$/NiAl(110) stacking (X_s and X_i refer to surface and interface species, respectively). In the following, this thin film will be denoted as 2L-alumina [23]. Its complex unit cell contains 92 atoms with Al_s bound either pyramidally or tetrahedrally, adapting a structure that cannot be clearly assigned to any bulk phase [23]. The unique structure and the nonstoichiometric nature of this 2L-alumina oxide layer recently raised questions regarding to what extent this surface oxide could be an approximant of γ-Al_2O_3 [15]. If the thickness of the alumina film could be increased, the influence of the substrate and the interface on the surface weakens, which is expected to result in alumina films that better represent the properties of bulk Al_2O_3 phases. Several routes to increase the thickness of 2L-alumina were studied previously: It was shown that metal clusters on 2L-alumina can bind and dissociate oxygen, which then spills over from the clusters and oxidizes the bimetallic substrate [27–29]. Further, oxidizing molecules such as water [30,31] and nitrogen dioxide [32,33] were shown

to adsorb, dissociate, and react with subsurface aluminum atoms. Exposure to water [31] and oxygen [34] in the millibar range or atomic oxygen [33] can significantly increase the oxide thickness, but these approaches do not result in ordered thin films. Previous routes for thicker crystalline films included deposition and subsequent oxidation of aluminum atoms [35] and the direct oxidation of the substrate [36]. These studies indicate the feasibility of growing ordered alumina films, but it appears to be difficult to balance the processes of oxidation, crystallization, atomic diffusion, and oxide decomposition in a favorable manner at one fixed temperature and chemical potential [36,37].

In this paper, we describe a method for the synthesis of thicker alumina films with excellent crystallinity on the NiAl(110) substrate: The as-grown 2L-alumina/NiAl(110) system is annealed in UHV at elevated temperatures to ensure a high degree of crystallographic order at the interface. The oxidation is continued after this at lower temperatures and higher oxygen pressures to increase the thickness and to avoid oxygen desorption. The film growth is monitored stepwise by x-ray photoelectron spectroscopy (XPS). The damping of the substrate peaks indicates the formation of a homogeneous overlayer. Low-energy electron diffraction (LEED) confirms excellent crystallinity. X-ray photoelectron diffraction (XPD) reveals changes in the atomic short-range order: While increasing the film thickness, the local formation of subnanometer-sized γ-$Al_2O_3(111)$ nuclei is observed. Surprisingly, the complex surface unit cell of the 2L-alumina film [18,23] is maintained when increasing the film thickness, implying that the new layers follow the arrangement of the interface layer. The subnanometer γ-$Al_2O_3(111)$ nuclei manifest themselves in the LEED pattern as hexagonal building blocks of octahedrally coordinated aluminum within the 2L-alumina unit cell. A spreading of these motifs is observed with increasing thickness of the oxide film, delivering an experimental contribution to elucidate the structure of the γ-$Al_2O_3(111)$ surface. Band structure measurements by angle-resolved photoelectron spectroscopy (ARPES) reveal no significant changes in the electronic structure upon increasing film thickness.

II. EXPERIMENT

The experiments were conducted in a modified VG ESCALAB 220 UHV system with a base pressure of 2×10^{-10} mbar [38]. The 2L-alumina films were prepared by oxidizing the clean NiAl(110) surface in 5×10^{-6} mbar oxygen at 530 K and subsequent annealing in UHV at 1150 K. The thickness of the thin films was increased systematically by oxidation in 10^{-5} mbar oxygen at 1050 K. Thicker films for the XPD study were grown at the same temperature, but at an oxygen pressure of 2×10^{-5} mbar. LEED was performed with a kinetic energy of $E = 64.5$ eV. XPS measurements were carried out at normal emission with a monochromatized Al Kα source, providing photons with an energy of $h\nu = 1486.6$ eV. The energy scale was calibrated as described in Ref. [39]. XPD patterns were collected with an unmonochromatized Si Kα source ($h\nu = 1740.0$ eV). The angle-resolved valence band spectra have been recorded with a helium discharge lamp (He Iα, $h\nu = 21.2$ eV).

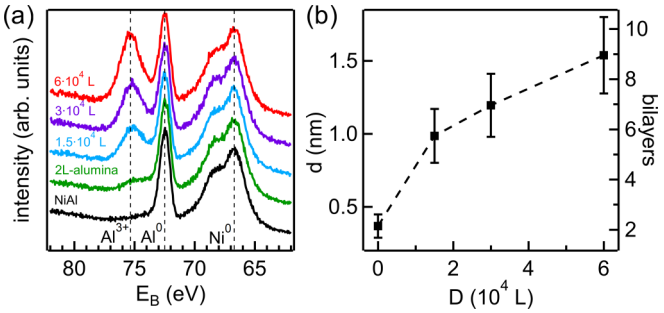

FIG. 1. (a) Al 2p and Ni 3p core level spectra of NiAl(110), 2L-alumina/NiAl(110), and of thicker alumina films on NiAl(110). An increase of the Al^{3+} signal indicates oxide formation. (b) Increase of the alumina film thickness vs. the total oxygen dosage D.

III. DATA AND DISCUSSION

Figure 1(a) shows the Al 2p and Ni 3p core level spectra for the different preparation steps during oxide growth. The spectrum of the NiAl(110) surface exhibits metallic Ni^0 and Al^0 peaks, to whose height all spectra are normalized. During the whole oxidation procedure these peaks and their ratios show no significant change, indicating that the supplied thermal energy is sufficient to enable diffusion inside the substrate. Oxidation of 2L-alumina films yields additional signals at higher binding energies which originate from Al_s^{3+} and interfacial Al_i^{2+} atoms [40]. With continued oxidation, the Al^{3+} intensity at a binding energy of 75.3 eV rises. The oxide thickness (d) is calculated by the intensity ratio of the oxidized Al species (I_O) and the metallic Al^0 peak (I_M) according to Eq. (1),

$$d = \lambda_O \cos(\theta) \ln\left[\frac{N_M \lambda_M}{N_O \lambda_O} \frac{I_O}{I_M \exp\left(\frac{d}{\lambda_O \cos(\theta)}\right)} + 1\right], \tag{1}$$

where θ refers to the electron emission angle with respect to the surface normal, λ_x to the inelastic mean free path, and N_x to the density of Al atoms in the material x. Equation (1) is similar to the one in Ref. [41] but additionally considers the observed attenuation of photoelectron intensity from the metal substrate below the oxide. λ_x is calculated with the Tanuma-Powell-Penn (TPP-2M) equation [42]. Figure 1(b) displays the evolution of the alumina thickness. After an oxygen dosage of 6×10^4 L, the film thickness increases from two atomic bilayers (0.4 nm) to nine atomic bilayers (1.5 nm). The indicated error bars are mainly attributed to uncertainties of λ_M [42]. A slight saturation behavior is observed, as the growth rate decreases according to the Cabrera-Mott theory for oxidation with increasing thickness [43]. However, further growth beyond 1.5 nm under the used experimental conditions appears possible.

Non-normalized spectra shown in Fig. S1 [44] illustrate the exponential attenuation of the two substrate peaks by the oxide overlayer. The resulting damping constant of 2.24 ± 0.07 nm is in good agreement with the calculated value of 2.67 ± 0.47 nm obtained from a continuous overlayer model with the inelastic mean free path from the TPP-2M equation [42,44–46]. This indicates a high degree of film uniformity

and flatness. A strong corrugation of the film surface would lead to substantially longer damping constants.

To gain insight about the short-range order, we employ angle-scanned XPD [47]. Figure 2(a) shows XPD patterns of the oxygen 1*s* peak from 2L-alumina and from a 1.0-nm-thick film, which were recorded at the corresponding peak maxima while subtracting the spectral background [Fig. 2(c), right panel]. At the given kinetic energy, mainly forward scattering contributes to the detected intensity modulation [47]. Due to the large unit cells involved in the system, and the concomitantly huge number of inequivalent oxygen emitter sites, we limit the modeling of these patterns to a simple forward scattering simulation, where all interatomic vectors originating from oxygen atoms are projected onto the unit sphere and represented in stereographic projection for comparison with the experimental data. The simulation is based on the structural models from Refs. [23,48]. The code considers a scaling of the total elastic scattering cross section as given by Browning *et al.* [49], an exponential intensity decrease with the distance between emitter and scatterer due to the inelastic scattering of electrons [42], and a decrease of the forward scattering amplitude with the square of the distance between the emitter and scatterer. A Gaussian blur of $\sigma_\theta = 5°$ and $\sigma_\phi = 5°/\sin(\theta)$ is used for the binning of the forward scattering maxima onto the same grid of polar and azimuthal angles as used for the data acquisition. The goal of these simulations is not a perfect reproduction of the measured XPD patterns, but to qualitatively reproduce the dominating features responsible for the photoelectron intensity modulation. When comparing these forward scattering calculations with experimental XPD data, the focus lies on the identification of dominant interatomic vectors within these highly complex surface structures.

In the case of 2L-alumina, and while neglecting weak interference fringes [50], oxygen emitters in the surface layer (O_s) should not contribute to the intensity modulation, but they contribute to the XPD pattern as scatterers. Likewise, oxygen atoms from the interface layer (O_i) contribute only as emitters and not as scatterers. Their photoelectrons undergo forward scattering at the aluminum and oxygen atoms in the surface layer (O_s and Al_s). Polar cuts for alumina films of different thicknesses are shown in Fig. 2(c). For 2L-alumina, the short-range order is dominated by tetrahedral and pyramidal building blocks [23], as shown in Fig. 2(d)(I) and (II). Tetrahedrally coordinated aluminum is also present in most bulk phases, however, the pyramidally coordinated aluminum can be regarded as a precursor of octahedrally coordinated aluminum [23]. For both of these building blocks, photoelectrons emitted from an O_i atom will undergo forward scattering at an Al_s atom on top, leading to the observed intensity increase at normal emission ($\theta = 0°$). As the blocks are highly distorted in 2L-alumina, the Al_s are not placed directly above O_i, leading to the small inner circle in the simulation [Fig. 2(b), left pattern]. For higher thicknesses, the feature at normal emission narrows significantly in the experimental data, indicating an increased local ordering.

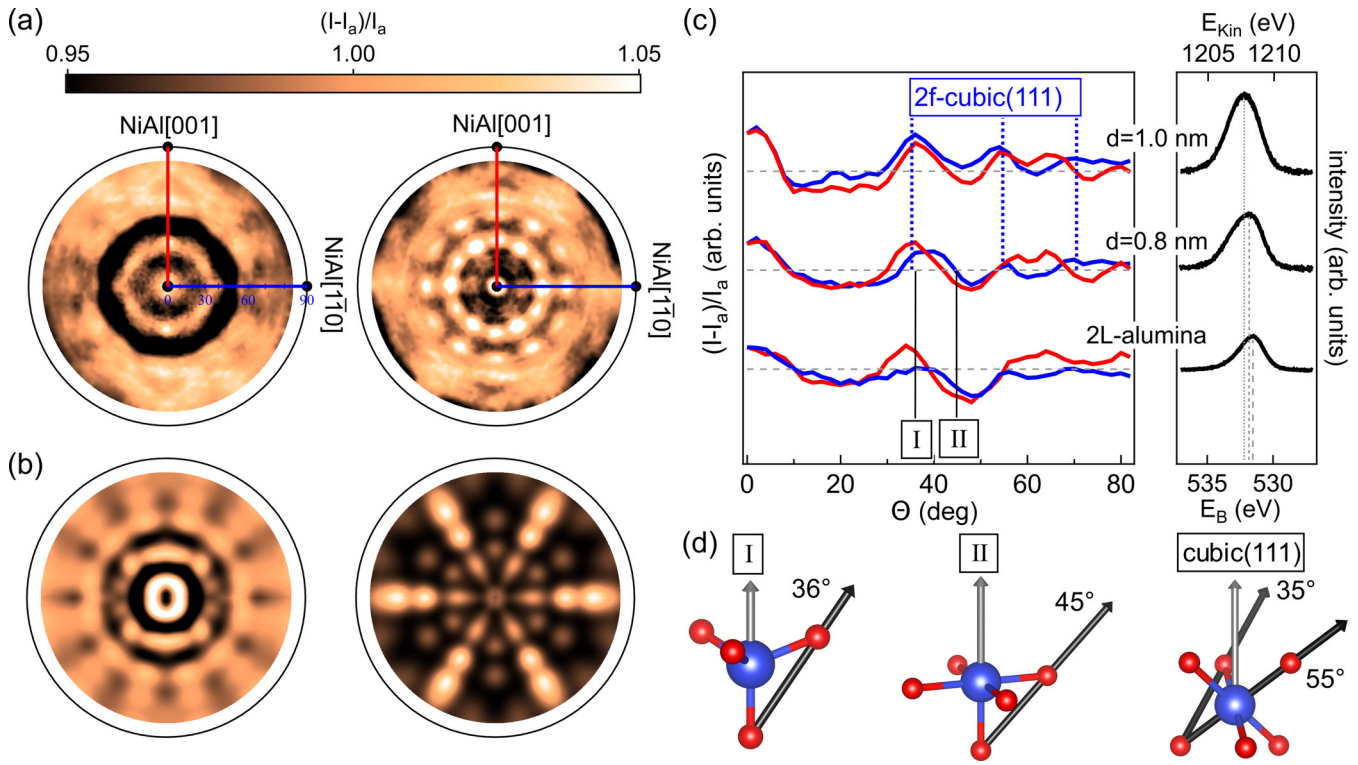

FIG. 2. (a) Experimental O 1*s* XPD pattern of 2L-alumina (left) and a 1.0-nm-thick film (right). (b) Forward scattering simulations of 2L-alumina (left) and γ-Al_2O_3(111) with a twofold symmetry (right). (c) Left: Polar cuts along the ⟨001⟩ and ⟨1$\bar{1}$0⟩ azimuthal directions of the NiAl(110) substrate [red and blue as marked in (a) for different film thicknesses]. In 2L-alumina, tetrahedral (I) and octahedral (II) building blocks are present [23]. For thicker films we observe the formation of a twofold cubic(111) structure. Right: Corresponding core level spectra. Dotted lines denote the intensity maxima. (d) Occurring building blocks as marked in (c). Oxygen and aluminum atoms are colored red and blue, respectively. The gray and black arrows indicate normal emission and forward scattering directions, respectively.

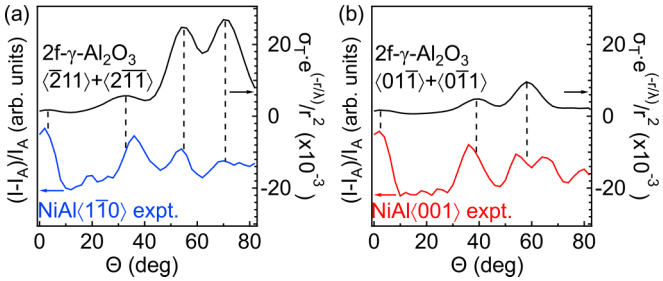

FIG. 3. (a) O 1*s* polar cut of the 1.0-nm-thick film along the $\langle 1\bar{1}0\rangle$ azimuthal direction of the NiAl(110) substrate [blue line, see Fig. 2(c)] compared with forward scattering calculations for γ-Al_2O_3(111) with a twofold symmetrization (black line, γ-$Al_2O_3\langle\bar{2}11\rangle$ and $\langle 2\bar{1}\bar{1}\rangle$ direction). (b) Corresponding polar cut along the $\langle 001\rangle$ azimuthal direction of the NiAl(110) substrate [red line, see Fig. 2(c)] compared with forward scattering calculations for γ-Al_2O_3(111) with a twofold symmetrization (black line, γ-$Al_2O_3\langle\bar{1}10\rangle$ and $\langle 1\bar{1}0\rangle$ direction).

In an ideal tetrahedral block (I), the photoelectrons from O_i will undergo forward scattering at O_s under an emission angle of $\theta = 36^\circ$. In the case of a pyramidal block (II), the ideal emission angle would be $\theta = 45^\circ$. Since the building blocks in 2L-alumina are highly distorted, the scattering angles range according to the model of Kresse *et al.* [23] from 30° to 40° for tetrahedral blocks and from 40° to 48° for pyramidal blocks [Fig. S2 [23,44]]. A clear forward scattering maximum is observed at $\theta = 34^\circ$ in the NiAl $\langle 001\rangle$ direction (red curve), which is caused by a preferred ordering of the tetrahedral blocks. For thicker films, a further increase of this signal is observed in the measured data, indicating the presence of more or better aligned tetrahedral blocks. The forward scattering maximum due to the pyramidal blocks occurs in 2L-alumina at 44° and can be observed best along the NiAl $\langle 1\bar{1}0\rangle$ direction [blue curve in Fig. 2(c) and Fig. S2(b) [23,44]].

For a 0.8-nm-thick alumina film the pyramidal signature is still present in the measured data [Fig. 2(c)], while typical scattering angles for a cubic(111) structure start to appear and become well recognizable for the 1.0-nm-thick film ($\theta = 0^\circ$, 35°, 55°, and 71°). This indicates that a critical thickness is required for the orientation change of the octahedral blocks from {100} to {111}. In Fig. 3 the polar cuts of the 1.0-nm-thick film from Fig. 2(c) are compared to forward scattering calculations of γ-Al_2O_3(111) with a twofold symmetrization [Fig. S3(b) [44,48,51,52]], which shows a better agreement than α-Al_2O_3(0001) [Fig. S3(c) [44,48,51,52]]. The scattering features of the γ-Al_2O_3 $\langle\bar{2}11\rangle$ and $\langle 2\bar{1}\bar{1}\rangle$ direction appear along the $\langle 1\bar{1}0\rangle$ azimuthal direction of the NiAl(110) substrate [Fig. 3(a)], and scattering features of the γ-Al_2O_3 $\langle 01\bar{1}\rangle$ and $\langle 0\bar{1}1\rangle$ direction are visible along the $\langle 001\rangle$ azimuthal direction of the substrate. The maximum at $\theta = 64^\circ$ can be attributed to an interference fringe [50].

After the orientation change of the octahedral blocks, the short-range order is thus best described as γ-Al_2O_3(111)-like. Forward scattering maxima along the $\langle 1\bar{1}0\rangle$ azimuthal direction of the NiAl(110) substrate [Fig. 3(a)] match well with those predicted for the bulk material. Differences between predicted and measured scattering angles might be attributed to further unconsidered bonds, interface-induced distortion, surface relaxation, or reconstruction. Further, it should be noted that the measured intensity anisotropies become significantly smaller for bigger polar angles θ. A reduced order between photoelectron emitters and scatterers in a larger distance is a reasonable interpretation, indicating the formation of small γ-Al_2O_3(111) nuclei.

The complex structure of the 2L-alumina film was previously resolved by using scanning tunneling microscopy and *ab initio* density functional theory [23]. Compared to the NiAl(110) substrate, the film has large unit cells and grows in two rotational domains, as shown in Fig. 4(a). The large real space lattice vectors of 2L-alumina lead to comparably small reciprocal lattice vectors. A complex LEED pattern shown in Fig. 4(b) is the result. The LEED pattern of a film with a thickness of 1.5 nm is shown in Fig. 4(c) and indicates that the symmetry of the 2L-alumina is maintained. The peak width does not change markedly, indicating that domain sizes in the homogeneous film do not change. In addition, a blurred hexagonal structure is observed. Figure 4(d) shows the difference of the normed intensities between Figs. 4(c) and 4(b). A marked intensity decrease is observed for the NiAl(110) (1×1) contribution, as the substrate is buried beneath a thicker oxide layer. An intensity enhancement is observed for the 2L-alumina lattice, which suggests that an increasing number of atoms form the corresponding unit cell. Further, this hexagonal structure also contributes to the intensity gain, with reciprocal lattice vectors $\vec{c}_1{}^*$ and $\vec{c}_2{}^*$ indicated in Fig. 4(d).

Figure 4(e) shows the line profile and a fit along the blue dashed line of Fig. 4(c). Several narrow peaks associated with the 2L-alumina unit cell are visible (green), and a comparatively broad peak (orange shaded) associated with the hexagonal structure. The reciprocal lattice constant is $k_\parallel = 2.55 \pm 0.02$ Å^{-1}, resulting in a real space lattice plane distance of 2.46 ± 0.02 Å and a lattice constant of 2.85 ± 0.02 Å. The fact that the peak of the hexagonal structure is rather broad indicates that the respective structural domains are on the subnanometer scale. Figure 4(f) displays circular line profiles, as marked in Fig. 4(c) by the red dashed line ($\sqrt{k^2_{\parallel 001} + k^2_{\parallel 1\bar{1}0}} = 2.55$ Å^{-1}) for different oxide thicknesses. Numerous narrow peaks from the 2L-alumina structure are visible in all line profiles. Further, six broad peaks are visible due to the hexagonal structure, with the sixth peak partly obstructed by the electron gun. This structure is visible for all examined thicknesses and can even be traced back to the 2L-alumina film, indicating that it is part of the bigger unit cell. By considering the known structure of 2L-alumina [23], we attribute the hexagonal structure to a surface unit cell with one tetrahedrally bound Al_s atom and one O_s as depicted in Fig. 4(g).

Smrčok *et al.* [48] proposed a model of the bulk γ-Al_2O_3 structure. We find a possible planar section along the [111] direction with an average oxygen-oxygen distance of 2.81 Å, as shown in the right inset of Fig. 4(g). The measured hexagonal structure shows a lattice constant between the one of the substrate and the one implied by the bulk oxide. As the overall crystal structure, the structures of the low index surfaces of γ-Al_2O_3 are still discussed controversially in literature [15,54] and based mostly on theoretical work [55–57]. Figure 4(h) depicts the structural motifs of the thin film after the orientation change of the octahedral building blocks: The local ordering

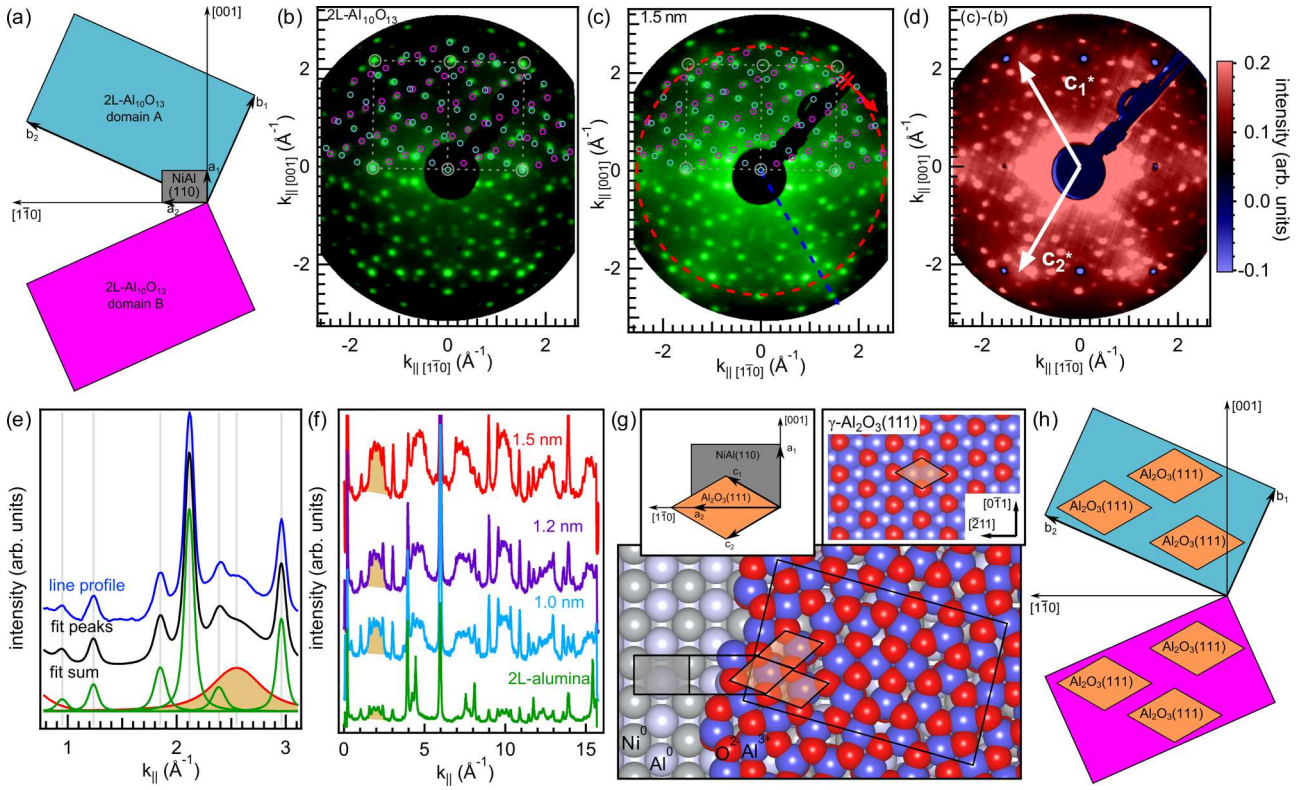

FIG. 4. (a) Dimension and domains of the 2L-alumina surface unit cell with respect to the NiAl(110) substrate ($a_1 = 2.89$ Å, $a_2 = 4.08$ Å, $\sphericalangle(a_1,a_2) = 90°$, $b_1 = 10.6$ Å, $b_2 = 17.9$ Å, $\sphericalangle(b_1,b_2) = 88.6°$, $\sphericalangle(a_2,b_2) = 24.1°$ [53]). (b) LEED pattern of 2L-alumina/NiAl(110). The theoretical pattern is indicated in the top half, with red and blue circles representing spots of the two domains as defined in (a). (c) LEED pattern of a film with a thickness of 1.5 nm. (d) Intensity difference pattern between (c) and (b). We observe an intensity decrease (blue) of the NiAl(110) substrate spots as well as a signal gain (red) belonging to the 2L-alumina pattern and a new and diffuse hexagonal structure. Reciprocal lattice vectors of the hexagonal phase are indicated. (e) Line profile (blue) as marked in (c) with a blue dashed line and corresponding fit (black). Green fit peaks belong to the large 2L-alumina unit cell. The broad orange-shaded peak is attributed to the hexagonal structure with a maximum at $k_{\parallel} = 2.55$ Å^{-1}. (f) Line profiles along the dashed red circle in (c) for $\sqrt{k^2_{\parallel 001} + k^2_{\parallel 1\bar{1}0}} = 2.55$ Å^{-1} for different thicknesses. The hexagonal structure exhibits broad peaks (one is shaded in orange), indicating domain sizes on the subnanometer scale. Furthermore, numerous sharper peaks are visible belonging to the 2L-alumina pattern. (g) Model of the hexagonal structure based on the 2L-alumina/NiAl(110) structure of Ref. [23]. The left inset shows the found unit cell with respect to the substrate. The right inset shows a model of γ-Al_2O_3 terminated along the [111] direction. (h) Structural model of the thin film after the orientation change of the octahedral blocks and the formation of γ-Al_2O_3(111) nuclei.

can be best described by subnanometer-sized γ-Al_2O_3 nuclei. These nuclei are formed inside of the homogeneous film and are arranged as parts of a bigger unit cell. This unit cell is the same as in the case of 2L-alumina and is thus implied by the interface.

In a recent study an anomalous hexagonal superstructure of alumina was found by scanning tunneling microscopy after two cycles of oxidation of 2L-alumina at 550 K and annealing at 920 K [58]. Krukowski *et al.* [58] found a hexagonal arrangement with a periodicity of 2.7 ± 0.2 Å. The similar lattice constant indicates that this structure is closely related to the hexagonal structure we identified in Fig. 4. A different approach for growing alumina thin films of variable thickness on NiAl(110) is the direct oxidation of the substrate at the annealing temperature [36,59], but it appears to be difficult to balance the processes of oxidation, crystallization, atomic diffusion, and oxide decomposition in a favorable manner at one fixed chemical potential and temperature. High temperatures are required for sufficient diffusion of Al atoms in the substrate [20] and for crystallization. However, thicker films might not be stable at a given temperature, as the adhesion energy at the interface provides extra stabilization only for thinner films [60]. This interface energy, on the other hand, increases the crystallization temperature of the thinner film [61]. Our approach combines both of these principles: The 2L-alumina system and thus the interface is crystallized at higher temperatures. After this, thicker films are grown at lower temperatures where they are more stable and the crystallization energy is lower. The thermal energy is still sufficient to allow atomic diffusion and to avoid Al depletion in the substrate.

Figure 5(a) shows ARPES data measured on 2L-alumina and on a 1.5-nm-thick film. Energy distribution curves for the metal substrate and alumina films of different thicknesses at the high symmetry points of the substrate surface Brillouin zone (SBZ) are displayed in Fig. 5(b). $3d$ states of the NiAl(110) substrate appear at $E - E_F < 4$ eV [18,62]. After oxidation, additional states appear at $E - E_F > 4$ eV, forming the valence bands of alumina, which are mainly of antibonding

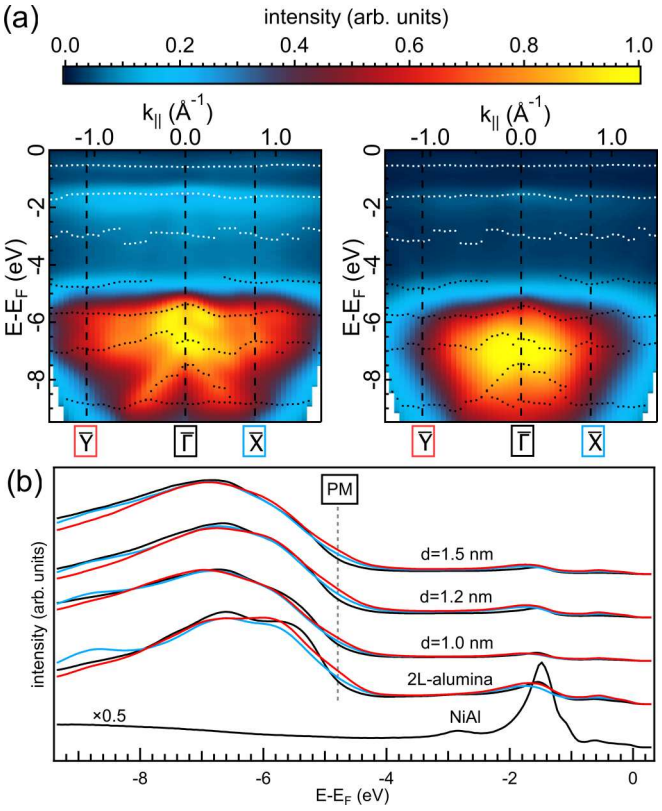

FIG. 5. (a) ARPES data from 2L-alumina (left) and from a 1.5-nm-thick film (right). Identified bands of the NiAl(110) substrate and of alumina (obtained by following local minima in the second derivative in Fig. S4 [44]) are marked with white and black dots, respectively. (b) Energy distribution curves (normalized to their integral) at $\bar{\Gamma}$ (black), $\bar{Y}$ (red), and $\bar{X}$ (blue) of the substrate surface Brillouin zone. The peak maximum (PM) of the valence band with minimum binding energy is indicated by a gray dashed line.

oxygen $2p$ character [63,64]. The measured band structure of 2L-alumina is in good agreement with previously published work [18]. Rather weak dispersions indicate comparably localized states. The valence band maximum of 2L-alumina is formed by a state of low spectral weight, best recognizable in the energy distribution curves recorded at the $\bar{Y}$ and $\bar{X}$ points of the substrate SBZ. The corresponding peak maximum is located with the second derivative in energy at $E - E_F = -4.7(9)$ eV and no clear dispersion is observed [Fig. S4 [44]]. As the valence band has a higher spectral weight at the $\bar{Y}$ point, the peak onset was determined at this position and is found to be $E - E_F = -4.2(4)$ eV [Fig. S5(a) [44]]. According to Krause *et al.* [65], this value describes the position of the valence band maximum, since it represents the fully relaxed state of the system. Previous work located the valence band onset at $E - E_F = -4.5$ eV [46], but did not consider this state. Changes in the spectral weight are observed for thicker films, however, within the experimental resolution no new bands are observed. The change of the valence band onset while increasing the thickness to 1.5 nm is 0.08 ± 0.09 eV [Fig. S5(a) [44]] and thus negligible. A slight work function decrease from $\phi = 4.1(6)$ eV to $\phi = 3.9(3)$ eV is observed [Fig. S5(b) [44]]. In total, we conclude that despite the structural changes, increasing the film thickness does not markedly change the valence band structure. This finding is of particular interest for the application of ultrathin alumina as a controlled tunneling barrier in prospective two-dimensional devices [66,67], especially when considering the recently demonstrated amorphous poly(methyl methacrylate) (PMMA)-assisted transfer of Al_2O_3-layers for highly stretchable and transparent transistors [68].

IV. SUMMARY

In summary, a multistep oxidation procedure is used to increase the thickness of 2L-alumina from two atomic layers to 1.5 nm. The resulting films are homogeneous and show excellent crystallinity. The large unit cell of 2L-alumina is maintained in the observed thickness range, indicating the fundamental importance of the interface for the ordering of successive layers. The atomic short-range order changes while adding additional atomic layers: Octahedral building blocks change their crystallographic direction from {100} to {111}, indicating the formation of subnanometer-sized γ-$Al_2O_3(111)$ nuclei arranged as compartments of the bigger 2L-alumina unit cell. Despite the structural changes, we find that while increasing the film thickness the band structure does not change significantly. Experimental evidence towards a surface model of γ-$Al_2O_3(111)$ is provided here by interpreting a hexagonal surface structure in the LEED pattern based on the 2L-alumina structure and finding structural analogies to γ-Al_2O_3. The resulting alumina films can be used as tunneling barriers in model studies, serve as a substrate to study the γ-$Al_2O_3(111)$-adsorbate interaction, and to elucidate the effect of the metal substrate on catalytic processes. The sequential preparation of the interface and the following layers opens a route to synthesize previously unknown thin film structures.

ACKNOWLEDGMENTS

We acknowledge helpful discussions with Thomas Greber and Zbynek Novotny and technical support by Thomas Kälin. This project has been financed under the University Research Priority Program LightChEC of the University of Zurich. G.M. acknowledges financial support by the Deutsche Forschungsgemeinschaft through SFB 1083 "Structure and Dynamics of Internal Interfaces."

[1] H.-J. Freund and G. Pacchioni, Oxide ultra-thin films on metals: New materials for the design of supported metal catalysts, Chem. Soc. Rev. **37**, 2224 (2008).

[2] J. Sauer and H.-J. Freund, Models in catalysis, Catal. Lett. **145**, 109 (2015).

[3] H.-J. Freund, Model studies in heterogeneous catalysis, Chem. Eur. J. **16**, 9384 (2010).

[4] G. Pacchioni and S. Valeri, *Oxide Ultrathin Films: Science and Technology* (Wiley, Hoboken, NJ, 2012).

[5] C. Freysoldt, P. Rinke, and M. Scheffler, Ultrathin Oxides: Bulk-Oxide-Like Model Surfaces or Unique Films? Phys. Rev. Lett. **99**, 086101 (2007).

[6] G. Pacchioni, L. Giordano, and M. Baistrocchi, Charging of Metal Atoms on Ultrathin MgO/Mo(100) Films, Phys. Rev. Lett. **94**, 226104 (2005).

[7] M. Sterrer, T. Risse, M. Heyde, H.-P. Rust, and H.-J. Freund, Crossover from Three-Dimensional to Two-Dimensional Geometries of Au Nanostructures on Thin MgO(001) Films: A Confirmation of Theoretical Predictions, Phys. Rev. Lett. **98**, 206103 (2007).

[8] M. Sterrer, T. Risse, U. M. Pozzoni, L. Giordano, M. Heyde, H.-P. Rust, G. Pacchioni, and H.-J. Freund, Control of the Charge State of Metal Atoms on Thin MgO Films, Phys. Rev. Lett. **98**, 096107 (2007).

[9] J. Repp and G. Meyer, Scanning tunneling microscopy of adsorbates on insulating films. from the imaging of individual molecular orbitals to the manipulation of the charge state, Appl. Phys. A **85**, 399 (2006).

[10] C. Freysoldt, P. Rinke, and M. Scheffler, Controlling Polarization at Insulating Surfaces: Quasiparticle Calculations for Molecules Adsorbed on Insulator Films, Phys. Rev. Lett. **103**, 056803 (2009).

[11] O. T. Hofmann, P. Rinke, M. Scheffler, and G. Heimel, Integer versus Fractional Charge Transfer at Metal(/Insulator)/Organic Interfaces: Cu(/NaCl)/TCNE, ACS Nano **9**, 5391 (2015).

[12] M. D. Kane, F. S. Roberts, and S. L. Anderson, Effects of alumina thickness on CO oxidation activity over Pd_{20}/alumina/Re(0001): Correlated effects of alumina electronic properties and Pd_{20} geometry on activity, J. Phys. Chem. C **119**, 1359 (2015).

[13] J. Zhou, J. Zhou, N. Camillone, and M. G. White, Electronic charging of non-metallic clusters: Size-selected Mo_xS_y clusters supported on an ultrathin alumina film on NiAl(110), Phys. Chem. Chem. Phys. **14**, 8105 (2012).

[14] M. F. Peintinger, M. J. Kratz, and T. Bredow, Quantum-chemical study of stable, meta-stable and high-pressure alumina polymorphs and aluminum hydroxides, J. Mater. Chem. A **2**, 13143 (2014).

[15] C. Bara, E. Devers, M. Digne, A.-F. Lamic-Humblot, G. D. Pirngruber, and X. Carrier, Surface science approaches for the preparation of alumina-supported hydrotreating catalysts, ChemCatChem **7**, 3422 (2015).

[16] G. Busca, The surface of transitional aluminas: A critical review, Catal. Today **226**, 2 (2014).

[17] T. N. Jensen, K. Meinander, S. Helveg, A. S. Foster, S. Kulju, T. Musso, and J. V. Lauritsen, Atomic Structure of a Spinel-Like Transition Al_2O_3(100) Surface, Phys. Rev. Lett. **113**, 106103 (2014).

[18] R. M. Jaeger, H. Kuhlenbeck, H.-J. Freund, M. Wuttig, W. Hoffmann, R. Franchy, and H. Ibach, Formation of a well-ordered aluminium oxide overlayer by oxidation of NiAl(110), Surf. Sci. **259**, 235 (1991).

[19] C. Becker, J. Kandler, H. Raaf, R. Linke, T. Pelster, M. Dräger, M. Tanemura, and K. Wandelt, Oxygen adsorption and oxide formation on Ni_3Al(111), J. Vac. Sci. Technol. A **16**, 1000 (1998).

[20] V. Maurice, G. Despert, S. Zanna, M.-P. Bacos, and P. Marcus, Self-assembling of atomic vacancies at an oxide/intermetallic alloy interface, Nat. Mater. **3**, 687 (2004).

[21] V. Rose, V. Podgursky, I. Costina, R. Franchy, and H. Ibach, High temperature oxidation of CoAl(100), Surf. Sci. **577**, 139 (2005).

[22] M. Antlanger, W. Mayr-Schmölzer, J. Pavelec, F. Mittendorfer, J. Redinger, P. Varga, U. Diebold, and M. Schmid, Pt_3Zr(0001): A substrate for growing well-ordered ultrathin zirconia films by oxidation, Phys. Rev. B **86**, 035451 (2012).

[23] G. Kresse, M. Schmid, E. Napetschnig, M. Shishkin, L. Köhler, and P. Varga, Structure of the ultrathin aluminum oxide film on NiAl(110), Science **308**, 1440 (2005).

[24] U. Diebold, S.-C. Li, and M. Schmid, Oxide surface science, Annu. Rev. Phys. Chem. **61**, 129 (2010).

[25] H.-J. Freund, N. Nilius, T. Risse, and S. Schauermann, A fresh look at an old nano-technology: Catalysis, Phys. Chem. Chem. Phys. **16**, 8148 (2014).

[26] A. Picone, M. Riva, A. Brambilla, A. Calloni, G. Bussetti, M. Finazzi, F. Ciccacci, and L. Du, Reactive metal-oxide interfaces: A microscopic view, Surf. Sci. Rep. **71**, 32 (2016).

[27] S. Shaikhutdinov, M. Heemeier, J. Hoffmann, I. Meusel, B. Richter, M. Bäumer, H. Kuhlenbeck, J. Libuda, H.-J. Freund, R. Oldman, S.D. Jackson, C. Konvicka, M. Schmid, and P. Varga, Interaction of oxygen with palladium deposited on a thin alumina film, Surf. Sci. **501**, 270 (2002).

[28] J. Sainio, M. Eriksson, and J. Lahtinen, Interaction of oxygen with chromium deposited on Al_2O_3/NiAl(110), Surf. Sci. **532**, 396 (2003).

[29] T. Wu, W. E. Kaden, W. A. Kunkel, and S. L. Anderson, Size-dependent oxidation of Pd_n ($n \leqslant 13$) on alumina/NiAl(110): Correlation with Pd core level binding energies, Surf. Sci. **603**, 2764 (2009).

[30] C.-W. Yi and J. Szanyi, D_2O adsorption on an ultrathin alumina film on NiAl(110), J. Phys. Chem. C **111**, 17597 (2007).

[31] A. Shavorskiy, K. Müller, J. T. Newberg, D. E. Starr, and H. Bluhm, Hydroxylation of ultrathin Al_2O_3/NiAl(110) films at environmental humidity, J. Phys. Chem. C **118**, 29340 (2014).

[32] T. Staudt, A. Desikusumastuti, M. Happel, E. Vesselli, A. Baraldi, S. Gardonio, S. Lizzit, F. Rohr, and J. Libuda, Modeling NO_x storage materials: A high-resolution photoelectron spectroscopy study on the interaction of NO_2 with Al_2O_3/NiAl(110) and BaO/Al_2O_3/NiAl(110), J. Phys. Chem. C **112**, 9835 (2008).

[33] C.-W. Yi and J. Szanyi, BaO/Al_2O_3/NiAl(110) model NO_x storage materials: The effect of BaO film thickness on the amorphous-to-crystalline $Ba(NO_3)_2$ phase transition, J. Phys. Chem. C **113**, 716 (2009).

[34] C. Weilach, C. Spiel, K. Föttinger, and G. Rupprechter, Carbonate formation on Al_2O_3 thin film model catalyst supports, Surf. Sci. **605**, 1503 (2011).

[35] Y. Lykhach, V. Moroz, and M. Yoshitake, Formation of epitaxial Al_2O_3/NiAl(110) films: Aluminium deposition, Appl. Surf. Sci. **241**, 250 (2005).

[36] M. Yoshitake, T. Lay, and W. Song, Well-ordered ultra-thin Al_2O_3 film formation on NiAl(110) by high-temperature oxidation, Surf. Sci. **564**, 211 (2004).

[37] T. T. Lay, M. Yoshitake, and W. Song, Epitaxial growth of well-ordered ultra-thin Al_2O_3 film on NiAl(110) by a single-step oxidation, Appl. Surf. Sci. **239**, 451 (2005).

[38] T. Greber, O. Raetzo, T. J. Kreutz, P. Schwaller, W. Deichmann, E. Wetli, and J. Osterwalder, A photoelectron spectrometer for *k*-space mapping above the Fermi level, Rev. Sci. Instrum. **68**, 4549 (1997).

[39] M. P. Seah, Summary of ISO/TC 201 Standard: VII ISO 15472: 2001–surface chemical analysis–x-ray photoelectron spectrometers–calibration of energy scales, Surf. Interface Anal. **31**, 721 (2001).

[40] N. M. Martin, J. Knudsen, S. Blomberg, J. Gustafson, J. N. Andersen, E. Lundgren, H. H. Ingelsten, P.-A. Carlsson, M. Skoglundh, A. Stierle, and G. Kresse, High-resolution core-level spectroscopy study of the ultrathin aluminum oxide film on NiAl(110), Phys. Rev. B **83**, 125417 (2011).

[41] B. R. Strohmeier, An ESCA method for determining the oxide thickness on aluminum alloys, Surf. Interface Anal. **15**, 51 (1990).

[42] C. J. Powell and A. Jablonski, *NIST Electron Inelastic-Mean-Free-Path Database - Version 1.2* (National Institute of Standards and Technology, Gaithersburg, MD, 2010).

[43] N. Cabrera and N. F. Mott, Theory of the oxidation of metals, Rep. Prog. Phys. **12**, 163 (1949).

[44] See Supplemental Material at http://link.aps.org/supplemental/10.1103/PhysRevB.96.155420 for analysis of non-normalized core level spectra, for XPD simulations regarding 2L-alumina, for XPD simulations regarding bulk alumina phases, for the second derivative of ARPES data, and for the valence band onset and work function.

[45] C. J. Powell and A. Jablonski, Evaluation of calculated and measured electron inelastic mean free paths near solid surfaces, J. Phys. Chem. Ref. Data **28**, 19 (1999).

[46] S. Andersson, P. A. Brühwiler, A. Sandell, M. Frank, J. Libuda, A. Giertz, B. Brena, A. J. Maxwell, M. Bäumer, H.-J. Freund, and N. Mårtensson, Metal-oxide interaction for metal clusters on a metal-supported thin alumina film, Surf. Sci. **442**, L964 (1999).

[47] C. S. Fadley, Angle-resolved x-ray photoelectron spectroscopy, Prog. Surf. Sci. **16**, 275 (1984).

[48] Ľ. Smrčok, V. Langer, and J. Křesťan, γ-alumina: A single-crystal x-ray diffraction study, Acta Crystallogr. Sect. C **62**, 83 (2006).

[49] R. Browning, T. Z. Li, B. Chui, Jun Ye, R. F. W. Pease, Z. Czyewski, and D. C. Joy, Empirical forms for the electron/atom elastic scattering cross sections from 0.1 to 30 keV, J. Appl. Phys. **76**, 2016 (1994).

[50] J. Osterwalder, Structural effects in XPS and AES: Diffraction, in *Surface Analysis by Auger and X-Ray Photoelectron Spectroscopy*, edited by D. Briggs and J. T. Grant (IM Publications, Chichester, UK, 2003), Chap. 20.

[51] A. Vlad, A. Stierle, N. Kasper, H. Dosch, and M. Rühle, *In situ* x-ray study of the γ- to α-Al_2O_3 phase transformation during atmospheric pressure oxidation of NiAl(110), J. Mater. Res. Technol. **21**, 3047 (2006).

[52] E. E. Newnham and Y. M. de Haan, Refinement of the a Al_2O_3, Ti_2O_3, V_2O_3 and Cr_2O_3 structures, Z. Kristallogr. - Cryst. Mater. **117**, 235 (1962).

[53] J. Libuda, F. Winkelmann, M. Bäumer, H.-J. Freund, T. Bertrams, H. Neddermeyer, and K. Müller, Structure and defects of an ordered alumina film on NiAl(110), Surf. Sci. **318**, 61 (1994).

[54] L. Kovarik, A. Genc, C. Wang, A. Qiu, C. H. F. Peden, J. Szanyi, and J. H. Kwak, Tomography and high-resolution electron microscopy study of surfaces and porosity in a plate-like γ-Al_2O_3, J. Phys. Chem. C **117**, 179 (2012).

[55] A. Dyan, C. Azevedo, P. Cenedese, and P. Dubot, Electronic and atomic structure computation of disordered low index surfaces of γ-alumina, Appl. Surf. Sci. **254**, 3819 (2008).

[56] H. P. Pinto, R. M. Nieminen, and S. D. Elliott, *Ab initio* study of γ-Al_2O_3 surfaces, Phys. Rev. B **70**, 125402 (2004).

[57] M. Digne, P. Sautet, P. Raybaud, P. Euzen, and H. Toulhoat, Use of DFT to achieve a rational understanding of acid-basic properties of γ-alumina surfaces, J. Catal. **226**, 54 (2004).

[58] P. Krukowski, S. Chaunchaiyakul, Y. Minagawa, N. Yajima, M. Akai-Kasaya, A. Saito, and Y. Kuwahara, Anomalous hexagonal superstructure of aluminum oxide layer grown on NiAl(110) surface, Nanotechnology **27**, 455708 (2016).

[59] W. Song and M. Yoshitake, X-ray photoelectron spectroscopy and low-energy electron diffraction study on the oxidation of NiAl(110) surfaces at elevated temperatures, Thin Solid Films **464**, 52 (2004).

[60] C. T. Campbell, Transition Metal Oxides: Extra Thermodynamic Stability as Thin Films, Phys. Rev. Lett. **96**, 066106 (2006).

[61] M. Zacharias and P. Streitenberger, Crystallization of amorphous superlattices in the limit of ultrathin films with oxide interfaces, Phys. Rev. B **62**, 8391 (2000).

[62] S.-C. Lui, M. H. Kang, E. J. Mele, E. W. Plummer, and D. M. Zehner, Surface states on NiAl(110), Phys. Rev. B **39**, 13149 (1989).

[63] C.-K. Lee, E. Cho, H.-S. Lee, K. S. Seol, and S. Han, Comparative study of electronic structures and dielectric properties of alumina polymorphs by first-principles methods, Phys. Rev. B **76**, 245110 (2007).

[64] E. Menéndez-Proupin and G. Gutiérrez, Electronic properties of bulk γ-Al_2O_3, Phys. Rev. B **72**, 035116 (2005).

[65] S. Krause, A. Schöll, and E. Umbach, Determination of transport levels of inorganic semiconductors by ultraviolet and inverse photoemission, Phys. Rev. B **91**, 195101 (2015).

[66] A. K. Geim and I. V. Grigorieva, van der Waals heterostructures, Nature (London) **499**, 419 (2013).

[67] T. Niu and A. Li, From two-dimensional materials to heterostructures, Prog. Surf. Sci. **90**, 21 (2015).

[68] S. H. Chae, W. J. Yu, J. J. Bae, D. L. Duong, D. Perello, H. Y. Jeong, Q. H. Ta, T. H. Ly, Q. A. Vu, M. Yun, X. Duan, and Y. H. Lee, Transferred wrinkled Al_2O_3 for highly stretchable and transparent graphene-carbon nanotube transistors, Nat. Mater. **12**, 403 (2013).